Exploring single-layered SnSe honeycomb polymorphs for optoelectronic and photovoltaic applications

Bakhtiar Ul Haq,[1,2,*] S. AlFaify,[1,2,†] R. Ahmed,[3,4] Faheem K. Butt,[5] A. Laref,[6] and Mohd. Shkir[1]

[1]*Advanced Functional Materials & Optoelectronics Laboratory (AFMOL), Department of Physics, Faculty of Science, King Khalid University, P.O. Box 9004, Abha, Saudi Arabia*

[2]*Research Center for Advanced Materials Science (RCAMS), King Khalid University, Abha 61413, P.O. Box 9004, Saudi Arabia*

[3]*Department of Physics, Faculty of Science, Universiti Teknologi Malaysia, UTM Skudai, 81310 Johor, Malaysia*

[4]*Center for High Energy Physics, University of the Punjab, Quaid-e-Azam Campus, Lahore 54590, Pakistan*

[5]*Department of Physics, Division of Science and Technology, University of Education, College Road, Township, Lahore 54770, Pakistan*

[6]*Department of Physics and Astronomy, College of Science, King Saud University, Riyadh 11451, Saudi Arabia*

(Received 20 December 2017; revised manuscript received 6 February 2018; published 23 February 2018)

Single-layered tin selenide that shares the same structure with phosphorene and possesses intriguing optoelectronic properties has received great interest as a two-dimensional material beyond graphene and phosphorene. Herein, we explore the optoelectronic response of the newly discovered stable honeycomb derivatives (such as α, β, γ, δ, and ε) of single-layered SnSe in the framework of density functional theory. The α, β, γ, and δ derivatives of a SnSe monolayer have been found to exhibit an indirect band gap, however, the dispersion of their band-gap edges demonstrates multiple direct band gaps at a relatively high energy. The ε-SnSe, however, features an intrinsic direct band gap at the high-symmetry Γ point. Their energy band gaps (0.53, 2.32, 1.52, 1.56, and 1.76 eV for α-, β-, γ-, δ-, and ε-SnSe, respectively), calculated at the level of the Tran-Blaha modified Becke-Johnson approach, mostly fall right in the visible range of the electromagnetic spectrum and are in good agreement with the available literature. The optical spectra of these two-dimensional (2D) SnSe polymorphs (besides β-SnSe) are highly anisotropic and possess strictly different optical band gaps along independent diagonal components. They show high absorption in the visible and UV ranges. Similarly, the reflectivity, refraction, and optical conductivities inherit strong anisotropy from the dielectric functions as well and are highly visible-UV polarized along the cartesian coordinates, showing them to be suitable for optical filters, polarizers, and shields against UV radiation. Our investigations suggest these single-layered SnSe allotropes as a promising 2D material for next-generation nanoscale optoelectronic and photovoltaic applications beyond graphene and phosphorene.

DOI: 10.1103/PhysRevB.97.075438

I. INTRODUCTION

For the past decade, two-dimensional (2D) solid crystals have attracted remarkable attention for their unique features that are much needed for applications in optoelectronics, photonics, and thermoelectrics [1–3]. Their intriguing characteristics such as flexibility, transparency, and ultrathinness make them favorable over bulk materials in cutting-edge nanoscale technologies. The ultrathin geometrical structure of 2D materials leads to quantum confinement effects in a single direction that evolve many interesting features in the electronic and optical properties of 2D materials [1]. Among the 2D materials family, only single-layered graphene is particularly distinguished to revolutionize electronics and optoelectronics owing to its unique electronic band structure, exceptional electrical conductivity, and failure strength [4]. Unfortunately, pristine graphene comes with a critical limitation in terms of its intrinsic semimetallic nature. The lack of an energy gap makes pristine graphene unable to completely switch off the electric current that hinders its applications in advanced technologies such as field-effect transistors and computer chips [5,6].

This has stimulated great efforts to search for 2D materials with an appropriate energy band gap beyond graphene [6]. Persistent efforts have promptly led to the discovery of several new 2D atomic-layer materials with exotic electronic and optical properties, such as layered metal dichalcogenides (LMDCs) [7], silicone [8], hexagonal boron nitride (h-BN) [9,10], and phosphorene [11,12], to name a few. Among them, phosphorene or single-layered black phosphorus that crystallizes in an orthorhombic structure, exhibiting a moderate direct band gap and high carrier mobility, is of particular interest for future applications in nanoscale optoelectronics [12–17]. However, the intriguing potential of phosphorene is seriously limited by certain critical drawbacks such as environmental instability and large-scale fabrication for industrial applications [4]. Subsequently, IV-VI semiconductor monochalcogenides that share numerous similar physical properties with phosphorene have moved to the forefront of research.

These IV-VI monochalcogenides adopt a structure that is similar to that of phosphorene and thus have great promise for applications in optoelectronic and solar energy conversion devices [18–24]. Their energy band gaps fall in the visible range of the electromagnetic spectrum ($\sim$0.5$-$1.5 eV) and are likely capable of absorbing the light of the respective photon energies [22]. Moreover, the physical characteristics of these materials (particularly tin chalcogenides) can be tuned for

*bakhtiarjadoon@gmail.com
†sasaalfaify@hotmail.com

any desired application through structural modifications. For example, their optical characteristics have been greatly evolved and luminescence features have been added to their physical properties via a phase transformation, though introducing vacancies and defects [24]. Similarly, tin chalcogenides grown in single crystals have been reported to exhibit a high absorption coefficient above the fundamental absorption edge, and are capable of absorbing a significant part of the solar spectrum [22]. Among IV-VI monochalcogenides, layer structured tin selenide is of particular interest for its low cost and high chemical and environmental stability. The constituents of SnSe are relatively earth abundant and environmental friendly, which makes SnSe a promising replacement for the expensive and toxic chalcogenide systems containing Pb, Cd, Hg, etc. [20,21,25]. Moreover, SnSe has an energy band gap (∼0.90 eV indirect and ∼1.30 eV direct) that falls right in the range of optimal band gaps for solar cells ($E_g = 1.0-1.5$ eV) [18,26,27]. Bulk SnSe exhibits weak van der Waals forces between consecutive layers and strong covalent bonds within the layers that make the extraction of low-dimensional derivatives, such as monolayers and nanosheets, particularly easy [28]. Therefore, SnSe has been successfully fabricated in 2D geometries similar to that of phosphorene and has been found to be useful for photodetectors and photovoltaic applications [21,26,29].

To further improve the performance of low-dimensional SnSe in nanoscale electronic and optoelectronic devices, different derivatives of single-layered SnSe have been explored in recent years [18,21,26,30]. These nonstop efforts have consequently resulted in the discovery of several energetically stable honeycomb derivatives of SnSe, such as α-SnSe, β-SnSe, γ-SnSe, δ-SnSe, and ε-SnSe. These new species of 2D SnSe have been found to possess energy gaps falling in the visible range of the solar spectrum and are claimed to be a potential source of sustainable energy production in terms of high thermoelectric efficiency [2]. Thus, with structural morphologies analogous to phosphorene, and band gaps overlapping with a visible range of the solar spectrum, it is reasonable to predict these novel single-layered SnSe polymorphs as potential materials for optoelectronic applications. However, an analysis of their potential for optoelectronic and solar energy applications has yet to be assessed. Therefore, a comprehensive study of the electronic and optical properties of this family of SnSe monolayers is mandatory to rate their capacity for applications in photovoltaic and optoelectronic devices, as tin chalcogenides have received great interest for optoelectronic applications in recent years [22–24].

Herein, we explore the electronic and optical properties of the five honeycomb derivatives of single-layered SnSe (α-SnSe, β-SnSe, γ-SnSe, δ-SnSe, and ε-SnSe) using the full-potential linearized augmented plane waves plus local-orbital [FP-L(APW + lo)] method within density functional theory (DFT). The electronic band structures/band gaps of the considered materials have been determined with the Tran-Blaha modified Becke-Johnson (TB-mBJ) [31–33] in addition to the generalized gradient approximations parametrized by Perdew-Burke-Ernzerhof (PBE-GGA) [34]. The present study of the optoelectronic properties of these single-layered SnSe polymorphs is believed to unveil their promise for photovoltaic and optoelectronic applications and will serve as a valuable reference for future experimental studies.

II. COMPUTATIONAL DETAILS

The present investigations of the electronic and optical properties of α-SnSe, β-SnSe, γ-SnSe, δ-SnSe, and ε-SnSe have been performed within the DFT-based FP-L(APW + lo) method. In this approach, the basis set is realized by dividing the unit cell into two parts: (i) the nonoverlapping spheres around the atoms, and (ii) the interstitial region. The wave functions are treated as atomiclike in the spherical region and plane-wave-like in the interstitial region. In the spherical region (muffin-tin spheres), wave functions have been expanded up to $l_{\max} = 10$, whereas the energy cutoff $K_{\max} = 8.0/R_{\mathrm{MT}}\ (\mathrm{Ryd})^{1/2}$ has been taken into account for the convergence of eigenvalues in the interstitial region. For the electronic band-structure calculations, the TB-mBJ together with PBE-GGA has been used respectively for the treatment of the exchange and correlation parts of the exchange-correlation energy. The TB-mBJ exchange potential has been reported to demonstrate a sufficiently accurate description of the electronic band structures/band gaps for semiconductors [32,35–43]. To quantify the spin-orbit coupling (SOC) effect, SOC based on the TB-mBJ (mBJ + SOC) has been included through the second variational procedure [44] to the present electronic structure calculations of single-layered SnSe polymorphs. The reduced muffin-tin values were chosen as 2.43 a.u. for Sn and 2.31 a.u. for Se atoms. The Fourier-expanded charge density was truncated at $G_{\max} = 16\,\mathrm{a.u.}^{-1}$. The Monkhorst-Pack special k-point approach [45] has been adopted for the integration of the Brillouin zone (BZ). The integrals over the special BZ are performed up to an $8 \times 8 \times 2$ k-point grid for good convergence of energy. The total energy was converged up to 10^{-5} Ryd/unit cell in the present self-consistent computations for well-defined results. These calculations with the provided computational details have been executed in the WIEN2K code [46].

In the calculations of the optical properties, the complex dielectric functions $\varepsilon(\omega) = \varepsilon_1(\omega) + i\varepsilon_2(\omega)$ have been determined with the TB-mBJ potential, where $\varepsilon_1(\omega)$ and $\varepsilon_2(\omega)$ are the real and imaginary parts of $\varepsilon(\omega)$. The dispersion of $\varepsilon_2(\omega)$ was obtained in the present electronic band-structure calculations through the momentum matrix elements and joint density of states (DOS) between the unoccupied and occupied eigenstates, and is solved using the following equation,

$$\varepsilon_2 = \frac{2e^2\pi}{\Omega\varepsilon_0} \sum_{K,V,C} \left|\psi_k^C \left|\hat{u}\cdot r\right| \psi_k^C\right|^2 \delta\left(E_k^C - E_k^V - E\right) \qquad (1)$$

$\varepsilon_1(\omega)$ is then derived from $\varepsilon_2(\omega)$ via the famous Kramers-Kronig transformations. The remaining optical parameters such as absorption [$\alpha(\omega)$], refractive index [$n(\omega)$], and reflectivity spectra [$R(\omega)$] are determined from $\varepsilon_1(\omega)$ and $\varepsilon_2(\omega)$ using the following standard equations,

$$\alpha(\omega) = \sqrt{2\omega}\left[\sqrt{\varepsilon_1(\omega)^2 + \varepsilon_2(\omega)^2} - \varepsilon_1(\omega)\right]^{\frac{1}{2}}, \qquad (2)$$

$$n(\omega) = \left[\sqrt{\varepsilon_1(\omega)^2 + \varepsilon_2(\omega)^2} + \varepsilon_1^2(\omega)\right]^{\frac{1}{2}} \Big/ \sqrt{2}, \qquad (3)$$

$$R(\omega) = \left|\frac{\sqrt{\varepsilon_1(\omega) + \varepsilon_2(\omega)} - 1}{\sqrt{\varepsilon_1(\omega) + \varepsilon_2(\omega)} + 1}\right|^2. \qquad (4)$$

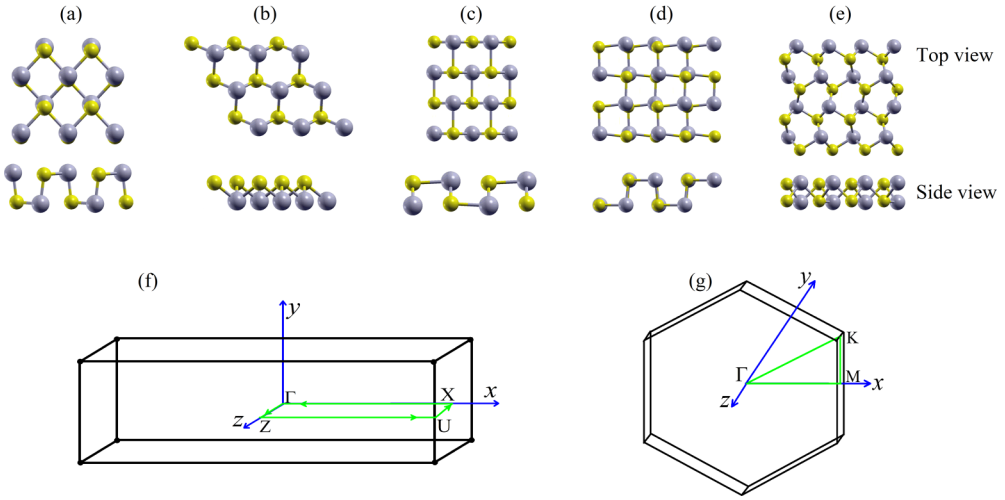

FIG. 1. Schematic of the geometric structures (top view and side view) of (a) α, (b) β, (c) γ, (d) δ, and (e) ε polymorphs of 2D SnSe. The gray and yellow balls represent the Sn and Se atoms, respectively. (f) The first BZ for α-, γ-, δ-, and ε-SnSe along the Γ-Z-U-X-Γ high-symmetry path. (g) The first BZ for β-SnSe along the Γ-M-K-Γ direction.

Comprehensive details of the calculation of the optical properties can be found elsewhere [47,48]. Since the integral over BZ requires a comparatively denser k mesh to get convergence in the calculations of the optical properties, a larger number of k points have been generated in a special BZ for the calculations of the optical properties. The high k points used in the special BZ for α-SnSe, β-SnSe, γ-SnSe, δ-SnSe, and ε-SnSe are 1360, 882, 1232, 1280, and 1200, respectively.

III. RESULTS AND DISCUSSION

The schematic geometric structures of α-SnSe, β-SnSe, γ-SnSe, δ-SnSe, and ε-SnSe are shown in Fig. 1. The structures of this class of SnSe monolayers correspond to individual layers in the bulk SnSe and therefore are believed to be equally stable [2]. These crystal structures hold strong anisotropy, except β-SnSe, which possesses an isotropic geometrical structure. Unlike the bulk structure that possesses an inversion point, the inversion symmetry is missing in these monolayers [49]. The missing inversion symmetry along with the spin-orbit coupling (SOC) results in a breaking of spin degeneracy in the electronic band structures of these single-layered polymorphs of SnSe, which will be discussed later. α-SnSe crystallizes as a rectangular-shaped lattice containing four atoms per unit cell. The geometry of α-SnSe corresponds to a puckered black-phosphorus-like structure having zigzag chains along the y axis. Similarly, γ-SnSe, δ-SnSe, and ε-SnSe adopt a rectangular-shaped lattice with four, eight, and eight atoms per unit cell, respectively. β-SnSe exhibits symmetrical lattice parameters along the x and y directions and contains two atoms per unit cell. It has a buckled surface analogous to that of blue phosphorus (β-P) [2]. The lattice constants, total energies per formula unit, and the formation energies of the derivatives of single-layered SnSe calculated in the present work with PBE-GGA are summarized in Table I. Our results are in good agreement with the available literature. The minor discrepancy can be attributed to the difference in the adopted methodologies.

The electronic band structures of α, β, γ, δ, and ε allotropes of SnSe monolayers determined with the TB-mBJ exchange potential are shown in Fig. 2. The significant differences in the band's dispersion seen in the electronic band structures of 2D SnSe polymorphs are due to the differences in their crystallographic directions. α-, β-, γ-, and δ-SnSe are found as indirect band-gap semiconductors with conduction band minima (CBM) located along the X-Γ, Γ-M, Γ-Z, and U-X directions, respectively, in the first BZ, whereas their valence band maxima (VBM) occur along the Γ-Z direction for α-SnSe, along K-Γ for β-SnSe, and along X-Γ for γ-SnSe and δ-SnSe. In contrast, the VBM and CBM for ε-SnSe occur at the same Γ in the first BZ. Thus, while the α, β, γ, and δ polymorphs of SnSe are indirect band-gap semiconductors,

TABLE I. The lattice constants, total energy per formula unit ($E_{\text{Formula-unit}}$), and the formation energies ($E_{\text{Formation}}$) of different polymorphs of the single-layered SnSe calculated with PBE-GGA in the present work in comparison with other calculations reported in Ref. [2].

	a (Å)		D (Å)		C (Å)			$E_{\text{Formation}}$ (eV)	
Material	Present	Other [2]	Present	Other [2]	Present	Other [2]	$E_{\text{Formula-unit}}$ (Ry)	Present	Others [2]
α-SnSe	3.98	3.95	2.60	2.59	4.77	4.82	−17218.7720	−4.96	−4.570
β-SnSe	3.90	3.78	1.53	1.53	3.90	3.78	−17218.5955	−3.56	−4.565
γ-SnSe	3.89	3.78	1.92	1.84	5.99	6.11	−17218.7676	−4.90	−4.555
δ-SnSe	6.25	6.14	2.61	2.59	6.18	6.23	−17218.6741	−3.63	−4.540
ε-SnSe	7.26	7.10	1.87	1.86	7.09	6.60	−17218.7694	−4.92	−4.510

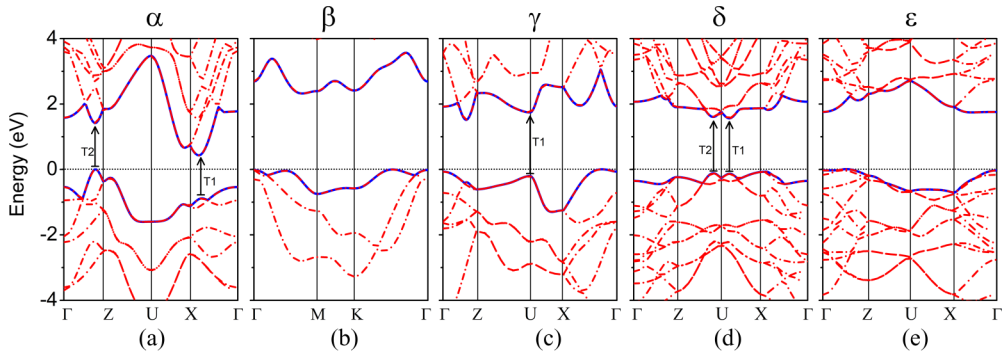

FIG. 2. The electronic band structures of (a) α, (b) β, (c) γ, (d) δ, and (e) ε polymorphs of 2D SnSe determined with the TB-mBJ potential. The fat blue bands are plotted along the valence band and conduction band edges. The arrowheads labeled as T1 and T2 in the band structures of α-, γ-, and δ-SnSe monolayers represent the possible direct optical transitions at the respective points in the BZ.

ε-SnSe is found to be a direct band-gap semiconductor with VBM and CBM simultaneously at the Γ point. Table II summarizes the positions of the VBM and CBM in k space for the five polymorphs. The calculated band gaps from the electronic band structures determined with PBE-GGA and TB-mBJ have been listed in Table III. Since the TB-mBJ potential has been established to reproduce sufficiently accurate energy band gaps of semiconductors within DFT, which is normally underestimated with common exchange-correlation functionals such as PBE-GGA, it is therefore the band structures obtained with PBE-GGA and TB-mBJ that are rather similar qualitatively, but the energy band gaps calculated with TB-mBJ are comparatively larger than those of PBE-GGA (Table III). However, the present electronic band-structure calculations within FP-L(APW + lo) are fairly comparable to those of the reported pseudopotential-based PBE-GGA and Heyd-Scuseria-Enzerhof approximation (HSE0) results in Ref. [2]. The minor discrepancy can be attributed to the different basis sets used. The energy band gaps of the current honeycomb derivatives of single-layered SnSe are mostly overlapping with the visible region of the solar spectrum. The band gap of β-SnSe is comparatively larger than that of other species due to the relatively smaller lattice constants.

To gain further insight into the electronic properties and realize the contribution from the different states into the electronic band structures, we determined the orbital-resolved electronic band structures for the five polymorphs of 2D SnSe [provided in the Supplemental Material (SM) 1 and 2 [51]]. The major role in the electronic band structures of 2D SnSe polymorphs has been found to be played by the p electrons from the Sn and Se atoms. The valence bands substantially stem from the Se-p electrons with a weak contribution from the Sn-s electrons, whereas the Sn-p states dominate the conduction bands. The p bands of Sn and Se further split into PX, PY, and PZ orbitals that exhibit different dispersions along independent diagonal components (see SM 2 [51]). The Sn-s electrons in the upper valence band carry out hybridization with p electrons from Sn and Se and develop sp bonds. These features are found to be nearly common to all the studied species of 2D SnSe.

Moreover, these honeycomb polymorphs mostly exhibit multiple valence and conduction band valleys, particularly β-SnSe and δ-SnSe, where other competing local VBM and CBM can be seen at energies close to those of the VBM and CBM. Such valleys open the possibilities of additional optical transitions for incident light photons having an energy that is slightly larger than their intrinsic band gaps. The band structures of the α, γ, and δ polymorphs exhibit additional coincident high-energy valence and conduction band valleys in k space that indicate possible direct optical transitions along these valleys at a relatively higher energy. The arrowheads designated as T1 and T2 in the electronic band structures (Fig. 2) indicate such high-energy direct band gaps and the possible direct optical transitions through them. The first potential direct band gap in α-SnSe occurring between the CBM and local VBM along the high-symmetry X-Γ direction (at 0.342, 0, 0) represented by T1 amounts to 1.31 eV, which is larger than the primary indirect gap by 0.87 eV. The orbital-resolved electronic band structures reveal this potential transition from Se-PZ in the VB to Sn-PZ in CB. Similarly, the second potential direct

TABLE II. The positions of valence band maxima and conduction band minima of α, β, γ, δ, and ε derivatives of 2D SnSe in k space along x, y, and z coordinates.

	VBM			CBM		
2D SnSe	k_x	k_y	k_z	k_x	k_y	k_z
α-SnSe	0	0	0.285	0.343	0	0
β-SnSe	0.242	0.139	0	0.240	0.416	0
γ-SnSe	0.128	0	0	0	0	0.191
δ-SnSe	0.262	0	0	0.271	0	0.215
ε-SnSe	0	0	0.131	0.139	0	0

TABLE III. The energy band gaps of α, β, γ, δ, and ε derivatives of 2D SnSe determined with PBE-GGA and TB-mBJ potentials in comparison with the available literature.

Band gaps	PBE-GGA	TB-mBJ	Nature of gap	Others
α-SnSe	0.41	0.53	Indirect	1.04 [2], 0.86 [50], 0.39 [50],
β-SnSe	2.29	2.32	Indirect	2.22 [2]
γ-SnSe	1.49	1.52	Indirect	1.52 [2]
δ-SnSe	1.37	1.56	Indirect	1.55 [2]
ε-SnSe	1.69	1.76	Direct	1.50 [2]

gap (of magnitude 1.42 eV) occurs between the Se-PY in the VBM orbital and the Sn-PY orbital in the local CBM along the Γ-Z direction (at 0, 0, 0.285), which is larger than the indirect band gap by a magnitude of 0.87 eV. In γ-SnSe, a direct energy gap of magnitude 1.95 eV occurs between the competing valleys at the high-symmetry U point (at 0.440, 0, 0.514). The VBM and CBM at the corresponding positions are defined by the Se-PY states and Sn-PY states, and hence are responsible for the predicted transition. The calculated direct energy gap in γ-SnSe is higher in energy than the indirect band gap by a magnitude of 0.42 eV. Similarly, δ-SnSe exhibits multiple competing valleys in the lower conduction band that are likely to lead to direct transitions along the Z-U (at 0.221, 0, 0.267) and U-X (at 0.271, 0, 0.215) directions. The predicted high-energy direct band gaps along the Z-U (T1) and U-X (T2) paths in BZ amount to 1.72 and 1.70 eV, respectively. T1 takes place while the excitation of electrons from the occupied Se-PZ states in the valence band to the available Sn-PZ states in the conduction band occurs, whereas T2 happens while the electrons from the Se-PX states in the valence band transfer to the Sn-PX states in the conduction band. The predicted direct band gaps T1 and T2 in δ-SnSe are larger than the principal indirect band gap by a magnitude of 0.16 and 0.14 eV, respectively. Thus a slight increase in energy beyond 1.65 eV can possibly trigger direct optical transitions in δ-SnSe along the Z-U and U-X directions. Similarly, the band structure of β-SnSe illustrates a potentially direct band gap from the Se-$PX + PY$ states to Sn-PZ states at the high-symmetry Γ point at a relatively high energy (Fig. 2). Hence, the 2D SnSe honeycomb polymorphs exhibit versatile band gaps overlapping with the visible range of the solar spectrum, anticipating their potential applications in photovoltaics and optoelectronics.

We further investigate the effect of spin-orbit coupling on the electronic band structures of the five 2D polymorphs of SnSe (shown in SM 1 [51]). Since these 2D SnSe monolayers lack inversion symmetry, the interplay of SOC and the missing inversion symmetry has resulted in a breaking of the spin degeneracy of the electronic band structures. The observed spin-orbit-induced spin splitting of the electronic band structures has been found to be directionally dependent and holds significant anisotropy (particularly the α, δ, and ε types of 2D SnSe) along the high-symmetry points in the BZ. They exhibit spin-degenerate bands along the Γ-Z direction, whereas there is significantly broken spin symmetry along the conduction band minima. The splitting of the conduction band minima has been recorded as 0.12, 0.06, 0, 0.03, and 0.10 eV for α-SnSe, β-SnSe, γ-SnSe, δ-SnSe, and ε-SnSe, respectively. The anisotropic spin-orbit splitting in these materials is likely interesting for applications in directionally dependent spin-transport devices. The spin splitting in the band structure of β-SnSe is relatively less directionally dependent due to its symmetrical structure. The band splitting due to SOC and missing inversion symmetry recorded in the present study are in agreement with that reported for monolayers of SnSe [49], GeSe [49], and MoS2 [52].

The effective masses of electrons summarized in Table IV have been extracted from the CBM using Eq. (5),

$$\frac{d^2E(k)}{dk^2} = \frac{\hbar^2}{m^*}. \tag{5}$$

TABLE IV. The effective masses of electrons extracted from the CBM for α, β, γ, δ, and ε derivatives of 2D SnSe in comparison with the available literature.

2D SnSe	m_e^*/m_0	Others
α-SnSe	0.11	0.13 [21], 0.17 [2]
β-SnSe	1.00	1.10 [2]
γ-SnSe	0.10	0.11 [2]
δ-SnSe	0.13	0.71 [2]
ε-SnSe	2.18	0.93 [2]

Equation (5) reveals that the effective masses are strongly dependent on the dispersion of CBM and are therefore found to be dissimilar for different polymorphs. They are the heaviest for ε-SnSe, followed by β-SnSe, due to their comparatively flatter CBM along the Γ and Γ-M high-symmetry directions. The effective masses of the electrons are found to be lighter for δ-SnSe for its CBM with relatively less curvature. Our results for the effective masses of electrons fairly match the available results. The minor discrepancy seen in our calculations with that of available results has been possibly driven by the difference in the methodologies used.

In addition, we determined the effective masses of electrons along different directions for the five polymorphs of 2D SnSe, as summarized in Table V. The anisotropy in the structure of the studied materials has been reflected in the electrons' effective masses along different directions. As seen in Table V, the calculated electrons' effective masses are as sensitively directionally dependent and thus predict anisotropic electron conductivity in these materials. A very similar trend of directional dependence of the electrons' effective masses has also been observed for bulk tin chalcogenides [53].

Next, we analyze the optical properties of the α, β, γ, δ, and ε derivatives of 2D SnSe determined with the TB-mBJ potential. As seen in Table III, the TB-mBJ potential has reproduced the electronic structures/band gaps with sufficient accuracy, so it is therefore reasonable to employ TB-mBJ for the calculations of the optical properties as they are directly associated with the electronic band structures. Similar to layered black phosphorus, the dielectric tensors of the considered species of 2D SnSe are highly anisotropic along the three independent crystallographic directions. The observed anisotropy in the optical spectra is the direct consequence of the difference in the crystallographic directions that govern dissimilarity in the band dispersion in the respective directions in the BZ.

TABLE V. The effective masses of electrons (m_e^*/m_0) calculated in different directions for α, β, γ, δ, and ε derivatives of 2D SnSe. d corresponds to the width of the monolayer.

2D SnSe	100	010	001	110	101	011	111
α-SnSe	0.24	d	0.15	0.24	0.12	0.14	0.12
β-SnSe	0.95	0.81	d	0.95	0.90	0.87	0.90
γ-SnSe	0.34	d	0.11	0.35	1.22	0.11	1.25
δ-SnSe	0.17	d	0.17	0.18	0.19	0.18	0.21
ε-SnSe	2.15	d	0.19	2.14	1.15	0.21	1.15

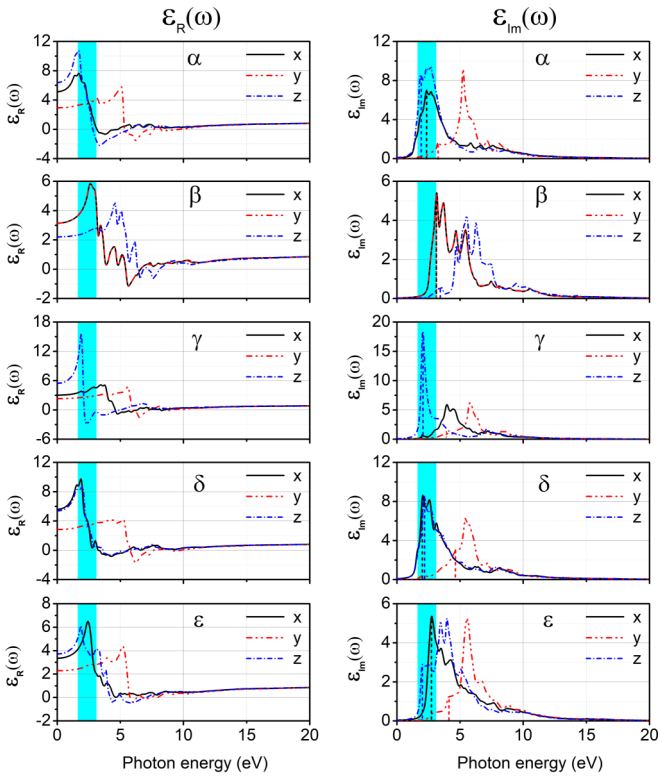

FIG. 3. The real and imaginary parts of dielectric functions against photon energy along the x, y, and z axis determined for α, β, γ, δ, and ε monolayer polymorphs of SnSe. The cyan-colored band represents the visible region of the electromagnetic spectrum.

Figure 3 shows the real part of the dielectric functions calculated for single-layered SnSe polymorphs. $\varepsilon_1(\omega)$ describes the electronic polarizability in solids in terms of static dielectric constants (the dielectric constant at the zero photon energy limits) through the Clausius-Mossotti relation. The static dielectric constants calculated for the five species of 2D SnSe are summarized in Table VI. As can be seen, α-SnSe and δ-SnSe exhibit relatively larger values of static dielectric constants, suggesting their relatively high polarizability. Moreover, the dispersion of $\varepsilon_1(\omega)$ adopts negative values for a specific range of energies depending on the type of 2D SnSe polymorphs. The positive values of $\varepsilon_1(\omega)$ correspond to the dielectric nature whereas the negative $\varepsilon_1(\omega)$ illustrates the metallic nature

TABLE VI. The static dielectric constants and plasmon's energy along the x, y, and z crystallographic directions for α, β, γ, δ, and ε derivatives of 2D SnSe.

	Static dielectric constants			Plasmon energies (eV)		
Polymorphs	x	y	z	x	y	z
α-SnSe	5.15	2.94	6.37	4.80	9.54	5.70
β-SnSe	3.15	3.15	2.21	6.60	6.60	8.09
γ-SnSe	3.04	2.33	5.45	8.39	9.10	4.94
δ-SnSe	5.60	2.85	5.38	5.56	7.60	5.70
ε-SnSe	3.35	2.29	3.72	4.61	7.47	6.95

of 2D SnSe. The negative values of $\varepsilon_1(\omega)$ typically span $\sim 4-9$ eV for the five polymorphs of 2D SnSe, demonstrating the metallic character of these materials in the UV part of the electromagnetic spectrum.

$\varepsilon_1(\omega)$ further provides information about the plasmon excitations that reportedly occur at energies corresponding to $\varepsilon_1(\omega) = 0$ and its first derivative is found to be positive [54,55]. Plasmons play an important role in determining the optical properties of semiconductors. Light photons with energies below the plasmon energies are reflected because the electric field associated with light is screened by electrons within the material, whereas those with energies above the plasmon's energies are transmitted since the electrons are unable to respond fast enough to screen the incident light. The calculated plasmon energies for the five species are summarized in Table VI and mostly occur in the UV range of the solar spectrum.

The $\varepsilon_2(\omega)$ of a dielectric tensor against the photon energy in the range of 0–20 eV is shown in Fig. 3. The peaks appearing in the imaginary parts $\varepsilon_2(\omega)$ correspond to the absorptive transitions from occupied states in the valence band to the unoccupied states in the conduction band. The major structures seen in the dispersion of $\varepsilon_2(\omega)$ along the independent diagonal components reflect multiple optical transitions between the valence and conduction bands. Below, we explain $\varepsilon_2(\omega)$ of the five species of 2D SnSe one by one.

The threshold energy of $\varepsilon_2(\omega)$ for α-SnSe is found to be equivalent for ε_{2xx} and ε_{2zz} whereas ε_{2yy} occurs at sufficiently larger energies. The first major optical transition in the electronic band structure (Fig. 2) of α-SnSe between VBM along the Γ-Z path and CBM along X-Γ has been depicted by a peak in ε_{2zz} at ~ 1.82 eV. Yet the first transition in α-SnSe occurs at a sufficiently higher energy than that of the separation between VBM and CBM (0.53 eV) and can be explained from the dispersion of the band structures with an indirect band gap in α-SnSe (see Fig. 2). Since the VBM and CBM in the band structure of α-SnSe are situated at a sufficiently larger distance in k space, the electrons in VBM need additional energy to be excited from VBM in Γ-Z to CBM along the X-Γ direction. An analysis of orbital-resolved band structures (see SM 2 [51]) shows the first transition to occur between the Se-4p (PY) in the VB to Sn-5P (PZ) orbitals in the conduction band. Similarly, the second major peak in ε_{2zz} appearing at 2.69 eV is believed to be the result of a direct transition from VBM to the local CBM along the Γ-Z direction (represented by T2 in Fig. 2). ε_{2xx} is defined by a broad structure that approaches to a maximum value at 2.35 eV and is attributed to the direct transition anticipated between the local VBM and CBM along X-Γ. The major peak in ε_{2yy}, however, occurs at higher energies in the UV range, demonstrating an optical transition at the corresponding energy.

β-SnSe exhibits multiple peaks in the dispersion of $\varepsilon_2(\omega)$, thus revealing multiple optical transitions for the particular dispersion of its VBM and CBM. As seen in Fig. 2, the energy gap edges in β-SnSe are relatively flatter and less dispersed against the energy window. Thus a slight increase in the photon energy allows electrons from VB to be excited to multiple competing points in the CB. The threshold energy at which $\varepsilon_2(\omega)$ in β-SnSe has been recorded is 2.33 eV for ε_{2xy}, which is fairly comparable to the separation in VBM along K-Γ

and CBM along the Γ-M direction. The first major transition in β-SnSe has been recorded at ∼3.14 eV and is believed to occur between VBM and CBM. The orbital-resolved electronic band structures (See SM 1 and 2 [51]) suggest this transition to be from the occupied Sn-s, Sn-PZ, and Se-PZ states in the valence band to the unoccupied Sn-$PX + PY$ and Se-PZ states in the conduction band. The second significant peak seen in the dispersion of ε_{2xy} at ∼3.67 stems from the optical transition from the VBM to the available Sn-$PX + PY$ and Se-$PX + PY$ states in the secondary CBM located at the K point, which is 91.30 meV higher in energy than the primary CBM (along Γ-M). Similarly, the other high-energy peaks in ε_{2xy} and ε_{2zz} of β-SnSe are associated with the optical transitions from the valence band to unoccupied states in the conduction band at higher energies.

The anisotropy in $\varepsilon_2(\omega)$ along the three diagonal components is particularly high in γ-SnSe owing to its considerably different band dispersions and crystallographic directions. The threshold energy of $\varepsilon_2(\omega)$ along the z axis corresponds to ∼1.54 eV, which is in good agreement with the calculated band gap (1.52 eV). ε_{2zz} is defined by a sharp peak with its maximum value at ∼2.02 eV and is attributed to the transition from Se-PX states in VBM to Sn-PY states in CBM. The major structure in $\varepsilon_2(\omega)$ along the x axis achieves an optimum value at ∼3.95 eV that can be attributed to the direct transition (represented by T1 in Fig. 2) from Se-PY in the valence band to Sn-PY states in the conduction band along the high-symmetry U point in the BZ. Similarly, ε_{2yy} exhibits its peak value at ∼5.74 eV corresponding to optical transitions at respective high energies.

The $\varepsilon_2(\omega)$ determined for δ-SnSe is found to be nearly isotropic along the x and z axis, however, significant anisotropy has been found along the y axis. A threshold energy of magnitude 1.48 eV has been found to be similar for both ε_{2xx} and ε_{2zz}. The predicted direct optical transitions in the band structure of δ-SnSe (represented by T1 and T2 in Fig. 2) have been seen in terms of peaks in the dispersion of ε_{2xx} and ε_{2zz}. Since the energy gaps represented by T1 and T2 exhibit a marginal difference, the corresponding peaks in ε_{2xx} and ε_{2zz} occur close to each other on the energy window. The dispersion of ε_{2xx} exhibits dual humps at 2.03 and 2.55 eV, whereas a single peak has been observed in ε_{2zz} at 2.17 eV. An analysis of the electronic band structure suggests an indirect transition between the Se-PX states in VBM and the Sn-PZ states in the CBM to be responsible for the peak at 2.03 eV in ε_{2xx}. The secondary peak in ε_{2xx} is attributed to the direct transition from Se-PZ states in the valence band to the Sn-PZ along the U-X direction represented by T1 in Fig. 2. The peak in ε_{2zz} at 2.17 eV is, however, characterized as a second possible direct transition (represented by T2) from the Se-PX states in the valence band to Sn-PX states in the conduction band along the Z-U direction.

Similarly, $\varepsilon_2(\omega)$ for ε-SnSe holds a high anisotropy along the x, y, and z axis and experiences a rapid increase in photon energy. The threshold energy for a ε_{2zz} equivalent to ∼1.75 eV is found to be relatively smaller than ε_{2xx} (∼2.14 eV) and ε_{2yy} (2.47 eV). The first optical transition between the VBM and CBM at the Γ point in ε-SnSe is reflected by a peak in ε_{2zz} at 2.02 eV. Moreover, the relatively flatter valence and conduction band edges along the Γ-Z and X-Γ directions with an additional valley in the conduction band along the Γ-Z direction (Fig. 2) allow multiple transitions from occupied states in the valence band to the unoccupied states in the conduction band. These potential transitions are encountered by multiple high-energy peaks in ε_{2xx} at 2.73, 3.48, and 4.26 eV, and in ε_{2zz} at 3.45 and 3.95 eV. As other polymorphs, the major peak in ε_{2yy} at 5.61 eV corresponds to excitations at higher energies.

TABLE VII. The optical band gaps and exciton binding energies along the x, y, and z axis determined for α, β, γ, δ, and ε derivatives of 2D SnSe.

	Optical band gap (eV)			Exciton binding energy (eV)		
2D SnSe	x	y	z	x	y	z
α-SnSe	2.34	3.25	1.87	1.81	2.72	1.34
β-SnSe	3.14	3.14	3.50	0.82	0.82	1.18
γ-SnSe	2.05	3.86	2.10	0.53	2.34	0.58
δ-SnSe	2.04	4.73	2.17	0.48	3.17	0.61
ε-SnSe	2.74	4.16	2.04	0.98	2.40	0.28

The optical band gaps [shown by vertical lines in the dispersion of $\varepsilon_2(\omega)$ in Fig. 3] derived from $\varepsilon_2(\omega)$ are highly anisotropic along the diagonal components (Table VII). The observed anisotropy in the optical gaps along the x, y, and z directions is particularly larger for α-SnSe and γ-SnSe. The difference in the optical gaps demonstrates that if the incident light with a photon energy between 1.87 and 3.25 eV shines on α-SnSe, the light polarized in the x and y diagonals will be absorbed. Similarly, the light polarized in the x direction will only be absorbed if the photon energy lies between 1.87 and 2.34 eV. Thus the 2D SnSe polymorphs reveal potential applications as polarization filters. The 2D-material-based polarization filter has already been realized in the case of black phosphorus [15,56].

The exciton binding energy is another important parameter in optoelectronics that associates the electronic band gap to the optical transitions in semiconductors. 2D semiconductors have been particularly praised for featuring larger exciton binding energies because of weak dielectric screening [21,57–59]. In the present first-principles electronic structure calculations, the exciton binding energies for the x, y, and z components have been estimated by taking the quantitative difference between the fundamental and optical band gaps. The excitonic binding energies summarized in Table VII present quantitative descriptions of the excitonic effects. The excitonic binding energies of the 2D SnSe polymorphs are relatively larger than those reported for SnSe single-layer (0.30, 0.27 eV), double-layer (0.20 eV), as well as several other 2D monochalcogenides reported in Refs. [21,49], and bulk (<0.01) SnSe [49]. The large excitonic binding energies of the 2D SnSe polymorphs, particularly α-SnSe and β-SnSe, show the great potential of these materials for nanoscale optoelectronic applications.

Figure 4 depicts the absorption spectra determined for α-, β-, γ-, δ-, and ε-SnSe. $\alpha(\omega)$ is directly associated with the electronic band structure/band gaps and inherits trends similar to that observed in $\varepsilon_2(\omega)$. In accordance with the calculated energy band gaps, the absorption edges occur in the infrared

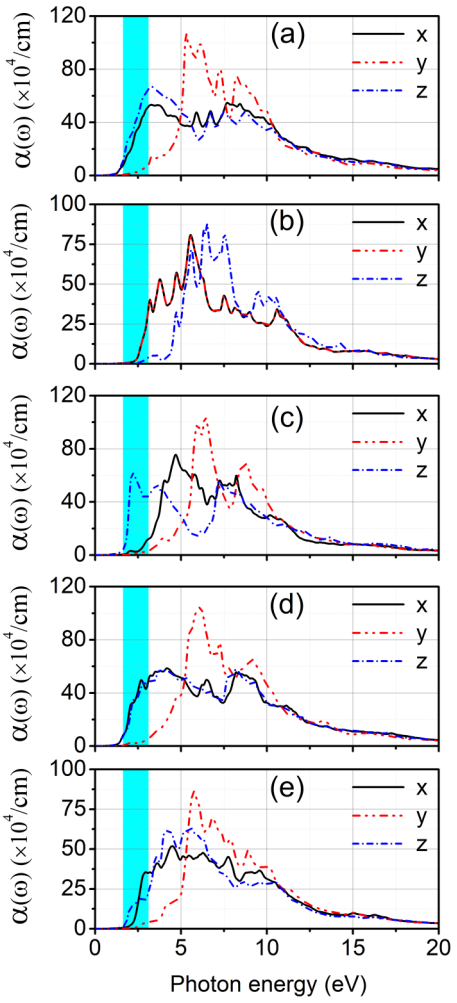

FIG. 4. The absorption spectra against photon energy along the x, y, and z directions determined for (a) α, (b) β, (c) γ, (d) δ, and (e) ε monolayer polymorphs of SnSe. The cyan-colored band represents the visible region of the electromagnetic spectrum.

range for α- and δ-SnSe and in the visible region for β-, γ-, and ε-SnSe. The absorption spectra of the currently studied 2D SnSe polymorphs fairly match the SnSe monolayer reported in Ref. [49]. Although, the optical absorption starts for light photons with energies falling in the infrared and visible range of the electromagnetic spectrum, it approaches its peak values in the UV range. $\alpha(\omega)$ is strictly different in the x, y, and z directions that reflect their superior polarization features, particularly in α, γ, and ε types of 2D SnSe. The observed anisotropy, as mentioned before, comes from the differences in the electronic band structures and crystallographic orientations along different diagonal components. A dramatically high anisotropy in $\alpha(\omega)$ has been seen for γ-SnSe, where the maximum absorption along the x component occurs in the visible range of the electromagnetic spectrum, whereas the absorption along the z component appears with an optimal value in the UV range. The highly anisotropic $\alpha(\omega)$ enables α, γ, and ε derivatives of 2D SnSe to absorb light photons along the supposedly x direction, but allows transferring them along the z direction. Hence, α, γ, and ε species of 2D SnSe are distinguished as potential materials for applications in cutting-edge nanoscale optoelectronic devices as polarizers and optical filters.

Figure 5 shows the reflectivity, refractive index, and optical conductivity of the SnSe allotropes. The reflectivity spectra of α-, β-, γ-, δ-, and ε-SnSe encounter a significant enhancement with an increase in photon energy. The optical reflection in these species of 2D SnSe occurs at energy intervals corresponding to negative $\varepsilon_1(\omega)$ (see Fig. 3) and major absorption (see Fig. 4), diminishing above their plasmon's energies summarized in Table VI. This implies that the propagation of electromagnetic waves vanishes at the corresponding energies and the reflection and absorption phenomena are dominated. The optical reflection in α-, β-, γ-, δ-, and ε-SnSe is highly polarized along independent crystallographic directions. In the visible-UV polarized reflectivity spectra of α-SnSe, y and z components with good reflection efficiency occur in the UV range, whereas there is an optimal x component in the visible range. In the case of β-SnSe, the reflectivity is isotropic along the x and y axis and appears with maximum values in the UV region for all diagonal components. Similar to α-SnSe, the reflectivity is polarized in the visible and UV regimes in the γ, δ, and ε polymorphs of SnSe monolayers. In γ-SnSe, it is dominated by the z component with its maximum value in the visible region, whereas optimal reflectivity along the x and y components appears in the UV range. The reflectivity spectra in δ-SnSe are nearly isotropic along the x and z components that appear in the visible region, whereas the UV range is favorable for reflectivity along the y components. Similarly, y and z components dominate the reflectivity in the case of ε-SnSe that appears in the UV region, whereas the x component, which is relatively lower in magnitude, appears in the visible region. The appearance of optimum reflection in the UV range is likely useful for application as shields against UV radiation in optoelectronics.

Figure 5 further shows the refractive indices $[n(\omega)]$ of the five polymorphs of single-layered SnSe against the photon energy. The common trend of strong anisotropy has also been observed for $n(\omega)$ that carries high anisotropy along independent diagonal components. The refractive index values explain the transparency of materials and thus describe their optical behavior for applications in optoelectronic devices. The optical medium is characterized by the refractive index such that $n \geqslant 1$ for transparent materials. The static refractive indices (refractive index at zero photon energy limits) along independent diagonal components have been summarized in Table VIII. All five 2D SnSe polymorphs show a maximum refraction in the infrared and visible regime of the solar spectrum, revealing their transparency at corresponding energies. However, their transparency vanishes in the UV range as the refractive indices experience an abrupt decline with photon energies that ultimately drops below unity for photon energies beyond ~7 eV. This can be understood from Fig. 4, where the absorption in 2D SnSe polymorphs approaches its maximum limits in the UV range. Being inversely proportional to the energy band gaps, the refractive indices are found to be comparatively larger for α-SnSe and δ-SnSe for their relatively narrower energy gaps. Moreover, the refractive index is dominated along the z direction in the case of α-SnSe and δ-SnSe. The refraction along the y axis (z axis for β) has been found to be comparatively lower in magnitude.

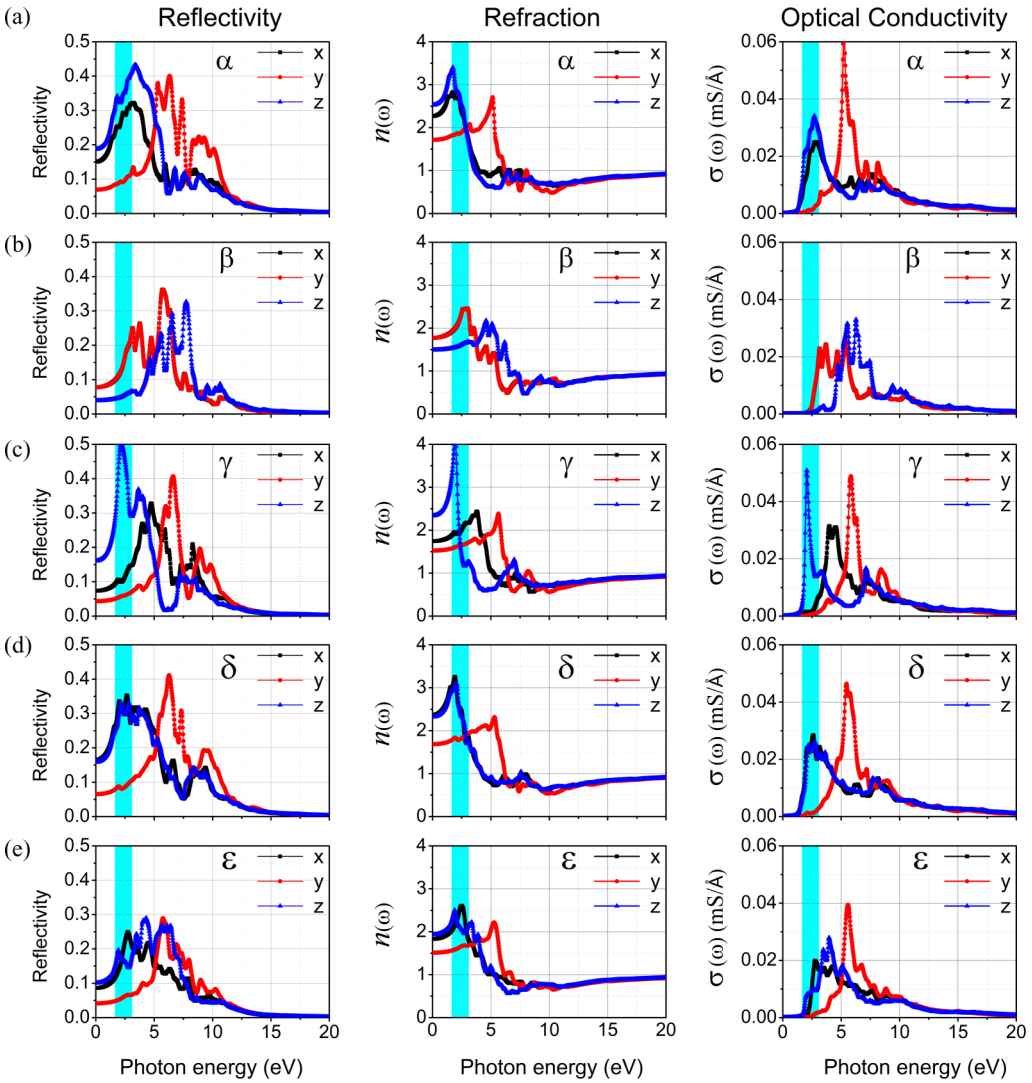

FIG. 5. The reflectivity spectra, refraction, and optical conductivity against photon energy along the x, y, and z directions determined for (a) α, (b) β, (c) γ, (d) δ, and (e) ε monolayer polymorphs of SnSe. The cyan-colored band represents the visible region of the electromagnetic spectrum.

Finally, we discuss the optical conductivity (real part) of α-, β-, γ-, δ-, and ε-SnSe, which has been directly calculated from the joint density of states. The threshold conductivity of α-, β-, γ-, δ-, and ε-SnSe occurs at energies equivalent to their respective band gaps. The peaks appearing in the dispersion of optical conductivity are mainly derived from the interband transitions. The trends in the dispersion of optical conductivity of α-, β-, γ-, δ-, and ε-SnSe are in good agreement with the rest of the optical parameters and possess strong anisotropy along the diagonal components. $\sigma(\omega)$ is typically dominated by y components (z component for β-SnSe) which occur in the ultraviolet region. The x and z components of $\sigma(\omega)$ are mostly centered in the visible or lower UV region due to the occurrence of band gaps in the corresponding energy. The peaks at a relatively low energy in $\sigma(\omega)$ reveal interband transitions between VBM and CBM. The optical conductivity is comparatively larger in α-SnSe than other polymorphs due to the small gap between the VBM and CBM. The spectral dependence of the optical conductivity of 2D SnSe polymorphs, particularly α-SnSe, is found in good agreement both qualitatively and quantitatively with the SnSe monolayer reported in Ref. [30].

TABLE VIII. The static refractive index of α, β, γ, δ, and ε derivatives of 2D SnSe.

	Refractive index		
2D SnSe	x	y	z
α-SnSe	2.27	1.72	2.52
β-SnSe	1.77	1.77	1.49
γ-SnSe	1.74	1.53	2.33
δ-SnSe	2.37	1.69	2.32
ε-SnSe	1.83	1.51	1.93

IV. CONCLUSION

In this article, we report the optoelectronic response of five honeycomb polymorphs (α, β, γ, δ, and ε) of single-layered

SnSe in the framework of the DFT-based FP-L(APW + lo) approach. α-, β-, γ-, and δ-SnSe were found semiconductors with an indirect band gap, however, secondary direct band gaps can be realized in these 2D materials at a relatively high energy. In contrast, ε-SnSe exhibits an intrinsic direct band gap along the high-symmetry Γ point. The energy band gaps of these polymorphs of the SnSe monolayer calculated at the level of TB-mBJ mostly overlap with the visible range of the solar spectrum and show a good potential for applications in solar cells. The dielectric functions of this family of SnSe monolayers are highly anisotropic along independent cartesian coordinates that have governed strong polarization in subsequent absorption, reflectivity, and refraction spectra. The optical band gaps evaluated from $\varepsilon_2(\omega)$ that are found to be strictly different along the cartesian coordinates are possibly advantageous for the polarization of light. Optimal absorption in these 2D materials occurs in the visible and UV parts of the spectrum and is highly anisotropic, particularly for the α, γ, and ε derivatives of 2D SnSe. This enables these materials to absorb light photons in a particular direction but allows them to transfer to others. Optimum absorption mostly appears in the UV range, which might be useful in fields where UV absorption is required. Similarly, they exhibit strictly different reflectivity and refraction properties along the x, y, and z components. The occurrence of optimal reflectivity in the UV range allows them to be used for applications as shields against UV radiation in optoelectronics. Thus, these 2D SnSe polymorphs possess superior polarization features and are useful for applications in nanoscale optoelectronic devices as polarizers and optical filters. Such rich features are suitable for applications in optoelectronic devices as optical filters and polarizers. Our investigations suggest these single-layered SnSe honeycomb polymorphs as highly qualified for next-generation optoelectronics and photovoltaic applications beyond phosphorene and graphene. We further believe that the optoelectronic properties of this family of SnSe monolayers can further be modified for more specific applications in future nanoscale optoelectronic and energy production devices via doping and strain engineering, etc.

ACKNOWLEDGMENTS

The authors would like to express their gratitude to Research Center of Advanced Materials - King Khalid University, Saudi Arabia for support. A.L. acknowledges financial support by a grant from the "Research Center of the Female Scientific and Medical Colleges," Deanship of Scientific Research, King Saud University.

[1] S. Zhang, M. Xie, F. Li, Z. Yan, Y. Li, E. Kan, W. Liu, Z. Chen, and H. Zeng, Semiconducting group 15 monolayers: A broad range of band gaps and high carrier mobilities, Angew. Chem. Int. Ed. **55**, 1666 (2016).

[2] Z.-Y. Hu, K. Li, Y. Lu, Y. Huang, and X. Shao, High thermoelectric performances of monolayer SnSe allotropes, Nanoscale **9**, 16093 (2017).

[3] D. Akinwande, N. Petrone, and J. Hone, Two-dimensional flexible nanoelectronics, Nat. Commun. **5**, 5678 (2014).

[4] V. Sorkin, Y. Cai, Z. Ong, G. Zhang, and Y. Zhang, Recent advances in the study of phosphorene and its nanostructures, Crit. Rev. Solid State Mater. Sci. **42**, 1 (2017).

[5] F. Li, X. Liu, Y. Wang, and Y. Li, Germanium monosulfide monolayer: A novel two-dimensional semiconductor with a high carrier mobility, J. Mater. Chem. C **4**, 2155 (2016).

[6] H. Zheng, X.-B. Li, N.-K. Chen, S.-Y. Xie, W. Q. Tian, Y. Chen, H. Xia, S. Zhang, and H.-B. Sun, Monolayer II-VI semiconductors: A first-principles prediction, Phys. Rev. B **92**, 115307 (2015).

[7] Q. H. Wang, K. Kalantar-Zadeh, A. Kis, J. N. Coleman, and M. S. Strano, Electronics and optoelectronics of two-dimensional transition metal dichalcogenides, Nat. Nanotechnol. **7**, 699 (2012).

[8] P. Vogt, P. De Padova, C. Quaresima, J. Avila, E. Frantzeskakis, M. C. Asensio, A. Resta, B. Ealet, and G. Le Lay, Silicene: Compelling Experimental Evidence for Graphenelike Two-Dimensional Silicon, Phys. Rev. Lett. **108**, 155501 (2012).

[9] C. Jin, F. Lin, K. Suenaga, and S. Iijima, Fabrication of a Freestanding Boron Nitride Single Layer and its Defect Assignments, Phys. Rev. Lett. **102**, 195505 (2009).

[10] L. Wang, B. Wu, J. Chen, H. Liu, P. Hu, and Y. Liu, Monolayer hexagonal boron nitride films with large domain size and clean interface for enhancing the mobility of graphene-based field-effect transistors, Adv. Mater. **26**, 1559 (2014).

[11] H. Liu, A. T. Neal, Z. Zhu, Z. Luo, X. Xu, D. Tománek, and D. Y. Peide, Phosphorene: An unexplored 2D semiconductor with a high hole mobility, ACS Nano **8**, 4033 (2014).

[12] L. Li, Y. Yu, G. J. Ye, Q. Ge, X. Ou, H. Wu, D. Feng, X. H. Chen, and Y. Zhang, Black phosphorus field-effect transistors, Nat. Nanotechnol. **9**, 372 (2014).

[13] J. Qiao, X. Kong, Z.-X. Hu, F. Yang, and W. Ji, High-mobility transport anisotropy and linear dichroism in few-layer black phosphorus, Nat. Commun. **5**, 4475 (2014).

[14] F. Xia, H. Wang, and Y. Jia, Rediscovering black phosphorus as an anisotropic layered material for optoelectronics and electronics, Nat. Commun. **5**, 4458 (2014).

[15] X. Wang, A. M. Jones, K. L. Seyler, V. Tran, Y. Jia, H. Zhao, H. Wang, L. Yang, X. Xu, and F. Xia, Highly anisotropic and robust excitons in monolayer black phosphorus, Nat. Nanotechnol. **10**, 517 (2015).

[16] J.-S. Kim, Y. Liu, W. Zhu, S. Kim, D. Wu, L. Tao, A. Dodabalapur, K. Lai, and D. Akinwande, Toward air-stable multilayer phosphorene thin-films and transistors, Sci. Rep. **5**, 8989 (2015).

[17] W. Zhu, M. N. Yogeesh, S. Yang, S. H. Aldave, J.-S. Kim, S. Sonde, L. Tao, N. Lu, and D. Akinwande, Flexible black phosphorus ambipolar transistors, circuits and AM demodulator, Nano Lett. **15**, 1883 (2015).

[18] P. D. Antunez, J. J. Buckley, and R. L. Brutchey, Tin and germanium monochalcogenide IV-VI semiconductor nanocrystals for use in solar cells, Nanoscale **3**, 2399 (2011).

[19] R. E. Abutbul, E. Segev, S. Samuha, L. Zeiri, V. Ezersky, G. Makov, and Y. Golan, A new nanocrystalline binary phase: Synthesis and properties of cubic tin monoselenide, CrystEngComm **18**, 1918 (2016).

[20] G. A. Tritsaris, B. D. Malone, and E. Kaxiras, Optoelectronic properties of single-layer, double-layer, and bulk tin sulfide: A theoretical study, J. Appl. Phys. **113**, 233507 (2013).

[21] L. Xu, M. Yang, S. J. Wang, and Y. P. Feng, Electronic and optical properties of the monolayer group-IV monochalcogenides MX (M = Ge, Sn; X = S, Se, Te), Phys. Rev. B **95**, 235434 (2017).

[22] S. Hegde, A. Kunjomana, K. Chandrasekharan, K. Ramesh, and M. Prashantha, Optical and electrical properties of SnS semiconductor crystals grown by physical vapor deposition technique, Physica B **406**, 1143 (2011).

[23] T. Raadik, M. Grossberg, J. Raudoja, R. Traksmaa, and J. Krustok, Temperature-dependent photoreflectance of SnS crystals, J. Phys. Chem. Solids **74**, 1683 (2013).

[24] P. Sutter, H.-P. Komsa, A. Krasheninnikov, Y. Huang, and E. Sutter, Luminescence of defects in the structural transformation of layered tin dichalcogenides, Appl. Phys. Lett. **111**, 262102 (2017).

[25] A. K. Singh and R. G. Hennig, Computational prediction of two-dimensional group-IV monochalcogenides, Appl. Phys. Lett. **105**, 042103 (2014).

[26] L. Li, Z. Chen, Y. Hu, X. Wang, T. Zhang, W. Chen, and Q. Wang, Single-layer single-crystalline SnSe nanosheets, JACS **135**, 1213 (2013).

[27] Q. Wang, W. Yu, X. Fu, C. Qiao, C. Xia, and Y. Jia, Electronic and magnetic properties of SnSe monolayers doped by Ga, In, As, and Sb: A first-principles study, Phys. Chem. Chem. Phys. **18**, 8158 (2016).

[28] F. Q. Wang, S. Zhang, J. Yu, and Q. Wang, Thermoelectric properties of single-layered SnSe sheet, Nanoscale **7**, 15962 (2015).

[29] S. Zhao, H. Wang, Y. Zhou, L. Liao, Y. Jiang, X. Yang, G. Chen, M. Lin, Y. Wang, and H. Peng, Controlled synthesis of single-crystal SnSe nanoplates, Nano Res. **8**, 288 (2015).

[30] L. C. Gomes, P. Trevisanutto, A. Carvalho, A. Rodin, and A. C. Neto, Strongly bound Mott-Wannier excitons in GeS and GeSe monolayers, Phys. Rev. B **94**, 155428 (2016).

[31] F. Tran and P. Blaha, Accurate Band Gaps of Semiconductors and Insulators with a Semilocal Exchange-Correlation Potential, Phys. Rev. Lett. **102**, 226401 (2009).

[32] D. Koller, F. Tran, and P. Blaha, Improving the modified Becke-Johnson exchange potential, Phys. Rev. B **85**, 155109 (2012).

[33] S. Azam, S. A. Khan, and S. Goumri-Said, Modified Becke-Johnson (mBJ) exchange potential investigations of the optoelectronic structure of the quaternary diamond-like semiconductors Li_2CdGeS_4 and Li_2CdSnS_4, Mater. Sci. Semicond. Process. **39**, 606 (2015).

[34] J. P. Perdew, K. Burke, and M. Ernzerhof, Generalized Gradient Approximation Made Simple, Phys. Rev. Lett. **77**, 3865 (1996).

[35] B. U. Haq, R. Ahmed, A. Shaari, F. E. H. Hassan, M. B. Kanoun, and S. Goumri-Said, Study of wurtzite and zincblende GaN/InN based solar cells alloys: First-principles investigation within the improved modified Becke-Johnson potential, Sol. Energy **107**, 543 (2014).

[36] B. U. Haq, A. Afaq, G. Abdellatif, R. Ahmed, S. Naseem, and R. Khenata, First principles study of scandium nitride and yttrium nitride alloy system: Prospective material for optoelectronics, Superlattices Microstruct. **85**, 24 (2015).

[37] B. U. Haq, M. B. Kanoun, R. Ahmed, M. Bououdina, and S. Goumri-Said, Hybrid functional calculations of potential hydrogen storage material: Complex dimagnesium iron hydride, Int. J. Hydrogen Energy **39**, 9709 (2014).

[38] B. Ul Haq, R. Ahmed, S. Goumri-Said, A. Shaari, and A. Afaq, Electronic structure engineering of ZnO with the modified Becke-Johnson exchange versus the classical correlation potential approaches, Phase Transitions **86**, 1167 (2013).

[39] B. U. Haq, R. Ahmed, and S. Goumri-Said, DFT characterization of cadmium doped zinc oxide for photovoltaic and solar cell applications, Sol. Energy Mater. Sol. Cells **130**, 6 (2014).

[40] B. U. Haq, R. Ahmed, J. Y. Rhee, A. Shaari, S. AlFaify, and M. Ahmed, Composition-induced influence on the electronic band structure, optical and thermoelectric coefficients of the highly mismatched GaNSb alloy over the entire range: A DFT analysis, J. Alloys Compd. **693**, 1020 (2017).

[41] B. U. Haq, R. Ahmed, M. Mohamad, A. Shaari, J. Rhee, S. AlFaify, M. B. Kanoun, and S. Goumri-Said, Engineering of highly mismatched alloy with semiconductor and semi-metallic substituent's for photovoltaic applications, Curr. Appl. Phys. **17**, 162 (2017).

[42] D. Koller, F. Tran, and P. Blaha, Merits and limits of the modified Becke-Johnson exchange potential, Phys. Rev. B **83**, 195134 (2011).

[43] F. Tran, P. Blaha, and K. Schwarz, Band gap calculations with Becke-Johnson exchange potential, J. Phys.: Condens. Matter **19**, 196208 (2007).

[44] A. MacDonald, W. Picket, and D. Koelling, A linearised relativistic augmented-plane-wave method utilising approximate pure spin basis functions, J. Phys. C: Solid State Phys. **13**, 2675 (1980).

[45] H. J. Monkhorst and J. D. Pack, Special points for Brillouin-zone integrations, Phys. Rev. B **13**, 5188 (1976).

[46] P. Blaha, K. Schwarz, G. Madsen, D. Kvasnicka, and J. Luitz, *WIEN2k, An Augmented Plane Wave+Local Orbitals Program for Calculating Crystal Properties* (Karlheinz Schwarz, Techn. Universität Wien, Austria, 2001).

[47] C. Ambrosch-Draxl, J. Majewski, P. Vogl, and G. Leising, First-principles studies of the structural and optical properties of crystalline poly (para-phenylene), Phys. Rev. B **51**, 9668 (1995).

[48] C. Ambrosch-Draxl and J. O. Sofo, Linear optical properties of solids within the full-potential linearized augmented planewave method, Comput. Phys. Commun. **175**, 1 (2006).

[49] G. Shi and E. Kioupakis, Anisotropic spin transport and strong visible-light absorbance in few-layer SnSe and GeSe, Nano Lett. **15**, 6926 (2015).

[50] L.-D. Zhao, S.-H. Lo, Y. Zhang, H. Sun, G. Tan, C. Uher, C. Wolverton, V. P. Dravid, and M. G. Kanatzidis, Ultralow thermal conductivity and high thermoelectric figure of merit in SnSe crystals, Nature (London) **508**, 373 (2014).

[51] See Supplemental Material at http://link.aps.org/supplemental/10.1103/PhysRevB.97.075438 for the effect of spin-orbit interactions in the electronic band structures, the orbital resolved band structures, and the PX, PY, and PZ components of p bands of Sn and Se.

[52] Z. Zhu, Y. Cheng, and U. Schwingenschlögl, Giant spin-orbit-induced spin splitting in two-dimensional transition-metal dichalcogenide semiconductors, Phys. Rev. B **84**, 153402 (2011).

[53] E. Sutter, Y. Huang, H.-P. Komsa, M. Ghorbani-Asl, A. Krasheninnikov, and P. Sutter, Electron-beam induced transformations of layered tin dichalcogenides, Nano Lett. **16**, 4410 (2016).

[54] M. Rocca, Low-energy EELS investigation of surface electronic excitations on metals, Surf. Sci. Rep. **22**, 1 (1995).

[55] K. Stahrenberg, T. Herrmann, K. Wilmers, N. Esser, W. Richter, and M. Lee, Optical properties of copper and silver in the energy range 2.5–9.0 eV, Phys. Rev. B **64**, 115111 (2001).

[56] L. Li, J. Kim, C. Jin, G. J. Ye, D. Y. Qiu, H. Felipe, Z. Shi, L. Chen, Z. Zhang, and F. Yang, Direct observation of the layer-dependent electronic structure in phosphorene, Nat. Nanotechnol. **12**, 21 (2017).

[57] B. R. Tuttle, S. M. Alhassan, and S. T. Pantelides, Large excitonic effects in group-IV sulfide monolayers, Phys. Rev. B **92**, 235405 (2015).

[58] D. Y. Qiu, H. Felipe, and S. G. Louie, Optical Spectrum of MoS_2: Many-Body Effects and Diversity of Exciton States, Phys. Rev. Lett. **111**, 216805 (2013).

[59] J.-H. Choi, P. Cui, H. Lan, and Z. Zhang, Linear Scaling of the Exciton Binding Energy Versus the Band Gap of Two-Dimensional Materials, Phys. Rev. Lett. **115**, 066403 (2015).